ACS Photonics

pubs.acs.org/journal/apchd5

Article

Substoichiometric Mixing of Metal Halide Powders and Their Single-Source Evaporation for Perovskite Photovoltaics

Published as part of the ACS Photonics virtual special issue "Photonics for Energy".

Quentin Guesnay,* Charles J. McMonagle, Dmitri Chernyshov, Waqas Zia, Alexander Wieczorek, Sebastian Siol, Michael Saliba, Christophe Ballif, and Christian M. Wolff*

Cite This: *ACS Photonics* 2023, 10, 3087−3094

Read Online

ACCESS | Metrics & More | Article Recommendations | Supporting Information

ABSTRACT: High-vacuum, single-source thermal evaporation is an appealing deposition process for perovskite photovoltaics. It promises the homogeneous and precisely controlled growth of very pure and homogeneous films on large areas in a conformal way. In this work, we study mechanically synthesized substoichiometric cesium bromide−lead iodide precursors, the single-source evaporation of the resulting mixes, subsequent deposited metal halide thin films, and converted perovskite thin films. Diffraction pattern analysis reveals the absence of new phases formed during ball-milling. Using synchrotron in situ grazing-incidence wide-angle X-ray scattering and energy-dispersive X-ray spectroscopy, we demonstrate that halide exchange between precursors occurs during the evaporation process. It is also found that a higher cesium bromide content results in films with more impurities. The proof-of-concept photovoltaic devices with the optimized cesium bromide content reach an efficiency of 15% for an optical bandgap of 1.7 eV.

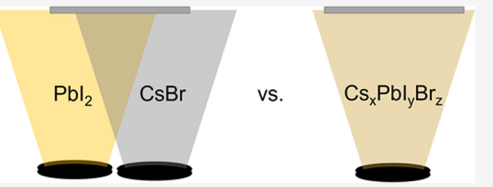

KEYWORDS: *physical vapor deposition, halide perovskites, grazing-incidence wide-angle X-ray scattering, single-source evaporation, solar cells*

INTRODUCTION

Vapor deposition processes are excellent candidates for photovoltaic device fabrication. A wide range of these techniques have been developed and mastered through decades of industrial development in numerous fields, e.g., in the semiconductor industry for light-emitting diodes, thin-film processing, etc. Applied to perovskite thin films, evaporation processing demonstrated its capability to coat large areas with highly homogeneous and conformal films.[1−4] Photovoltaic devices with high power conversion efficiencies above 20% were also demonstrated,[4,5] albeit for comparably small device areas (0.09−0.16 cm^2).

One of the most widely used vapor deposition technique is high-vacuum thermal evaporation. The evaporation of precursors in one or multiple crucibles in a high-vacuum chamber involves different advantages: high purity growth, precise rate and thickness control, and low risks of lead contamination. This evaporation technique is particularly well-suited for depositing the metal halide backbone of hybrid organic−inorganic halide perovskites. It is however more delicate to employ when organic precursors are used, resulting in the development of sequential processes of perovskite thin films.[6] They comprise the thermal evaporation of a metal halide template, followed by its conversion into the perovskite phase by the deposition of organohalides. This conversion can be obtained by any solution or vapor deposition technique.

Coevaporation of multiple precursors allows alloying, therefore fine-tuning the resulting thin film's characteristics. However, increasing the number of sources increases the overall complexity of the process: more signals to stabilize and control, cross-talking concerns, or sensitivity to single-signal fluctuations. In an attempt to simplify this process, we present here the mixing of substoichiometric metal halide precursors (lead iodide (PbI_2) and cesium bromide (CsBr)) and subsequent single-source evaporation of the resulting mixture. The mixture and its evaporation and deposition are studied via synchrotron grazing-incidence wide-angle X-ray scattering (GIWAXS). In situ GIWAXS allows tracking of the formation, fluctuation, and disappearance of the different crystalline phases during evaporation, as well as their orientation with respect to the substrate for the thin films once deposited. Readers interested in this technique are referred to the work of Held et al.[7] or the review of Qin et al.[8] Energy-dispersive X-ray spectroscopy (EDX) complements this structural information with chemical insights. The resulting metal halide templates

Received: March 31, 2023
Published: August 16, 2023

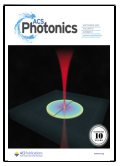

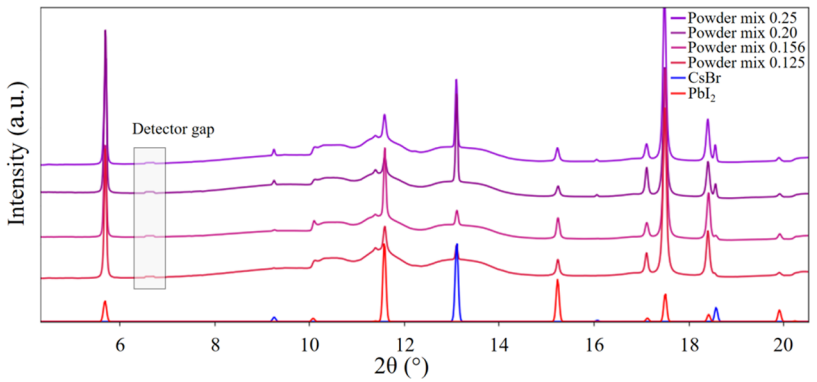

Figure 1. Powder diffractograms of the mixtures obtained by ball-milling. All of the powder mix diffractograms can be expressed as a linear combination of the diffractograms of CsBr and PbI_2, without the appearance of any third crystalline compound. Note: the patterns were collected via synchrotron X-ray diffraction with a beamline wavelength of 0.694 Å.

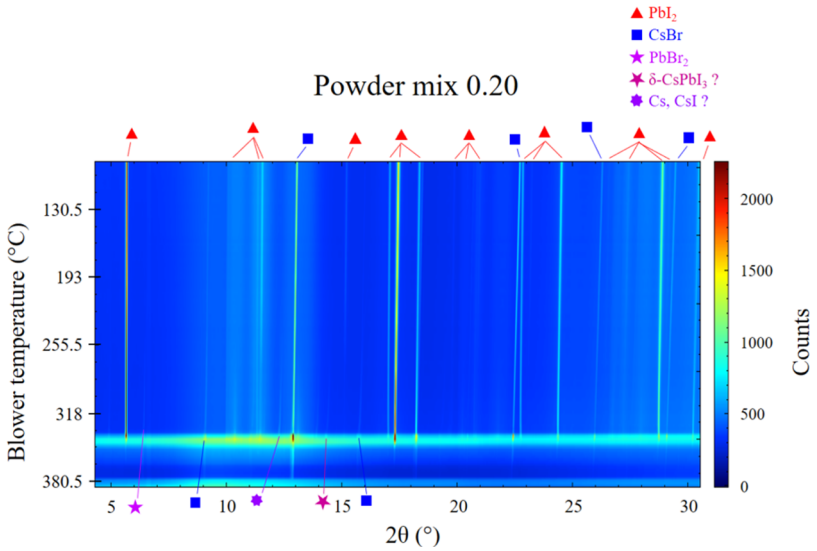

Figure 2. Temperature evolution of the integrated 2D GIWAXS map from 0.2 powder mix. Note: the patterns were collected via synchrotron X-ray diffraction with a beamline wavelength of 0.694 Å.

are then converted into perovskite thin films and implemented in photovoltaic devices.

RESULTS AND DISCUSSION

Powder Mixing and Evaporation. Lead iodide (PbI_2) and cesium bromide (CsBr) powders were mixed by ball-milling at different molar ratios (0.125, 0.156, 0.2, and 0.25 CsBr for 1 PbI_2). These compositions will be referred to as 0.125, 0.156, 0.20, and 0.25 powder mixes, respectively. The objective was to find a mixture that, once thermally evaporated in a single crucible, results in a thin film with a composition similar to our coevaporated template baseline.[9] The chemical composition of the latter corresponds to an approximate $Cs_{0.24}PbI_{2.2}Br_{0.25}$ in the resulting thin film, as measured with a self-consistent energy-dispersive X-ray spectroscopy (EDX) procedure detailed in the Methods section. The theoretical value expected from the evaporation rates forming compact films (0.1 Å/s CsBr/1 Å/s PbI_2) is 0.156 CsBr/1 PbI_2. This difference suggests a rearrangement during the evaporation and growth of the film.

The powder diffraction patterns of different CsBr/PbI_2 mixtures obtained by ball-milling are shown in Figure 1. The patterns with an extended range of angles (2θ = 2.5−36.5°) are available in the Supporting Information (Figure S1). Importantly, we did not observe a third crystalline phase in any of the different mixtures. This is a notable difference from other ball-milling reports in perovskite literature featuring the appearance of new phases.[10−16] For all diffractograms and the probed range of diffraction angles, all of the diffraction peaks can be ascribed to either PbI_2 or to CsBr. Here, the CsBr-associated signal appears increasingly pronounced corresponding to the precursor fraction. The diffractograms can be expressed as linear combinations of the reference diffractograms of CsBr and PbI_2, except for two prominent features: (1) The shoulder next to the PbI_2 (1 0 0) peak at 10° that is very likely caused by a stacking fault of the PbI_2 structure,[17] explained by the well-known polytypism nature of PbI_2,[18,19] accentuated by the attempt to intermix CsBr. (2) Three broad features (8−12, 12−14, and 17−18.5°) can be associated with the glass capillary. In the literature, Igual-Muñoz et al.[10] were reporting signs of a third perovskite phase after ball-milling the same precursors, albeit with a stoichiometric ratio of 1 CsBr/1 PbI_2. Rodkey et al.[11] documented the mass fraction evolution as a function of the ball-milling time with AgBr, CsBr, and $BiBr_3$ as precursors. After a few minutes, a decrease of the precursors' fractions and an increase in intermediate phases

https://doi.org/10.1021/acsphotonics.3c00438
ACS Photonics 2023, 10, 3087−3094

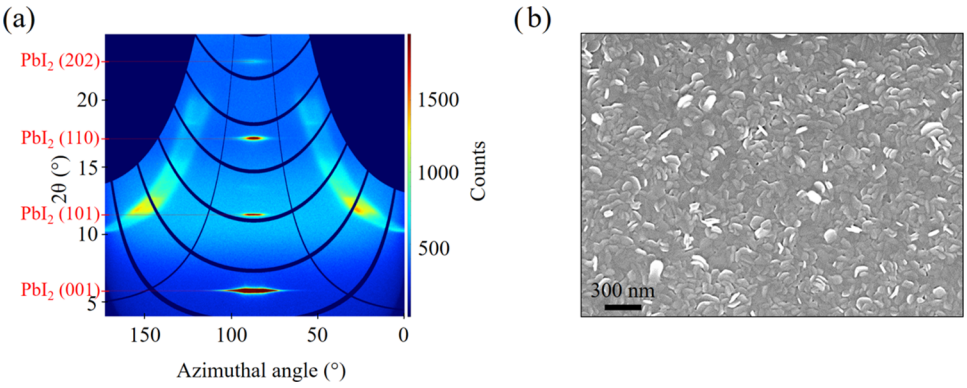

Figure 3. (a) Diffraction pattern as a function of the azimuthal angle of the metal halide thin film obtained by single-source evaporation of the 0.2 powder mix and (b) the corresponding SEM top view of the film.

(Cs_3BiBr_6, $Cs_3Bi_2Br_9$) were observed. Eventually, when approaching 1 h of mixing, the only contribution came from the desired $Cs_2AgBiBr_6$ perovskite phase. Li et al.[20] adjoined a salt melting step after the mechanical mixing of the powders (CsI + PbI_2, CsI + PbI_2 + $PbCl_2$, CsI + PbI_2 + $PbCl_2$+ $PbBr_2$) and were, according to their differential scanning calorimetry (DSC) measurements, able to obtain new phases distinct from the precursors, albeit without diffraction measurements to confirm the presence of a new crystallographic phase. All of the compositions investigated in this study feature a low cesium content (in the 0.1 Cs/1 Pb range).

After mixing, we studied the evaporation of the powder mixes via in situ synchrotron X-ray diffraction. A hot gas blower heated the glass capillary tube containing the powder mixes while acquiring the GIWAXS patterns. A schematic of the experiment is available in the Supporting Information (Figure S2). The capillary tube was furthermore connected to a turbo pump, which established a pressure in the 10^{-6} mbar range, conventional values for thermal evaporation. In the following, the 0.2 mix is shown, as the behavior is qualitatively similar for all mixtures. The data of the other mixes are available in the Supporting Information (Figure S3), complemented by a temperature evolution of the 2D GIWAXS map showing the evaporation.

Figure 2 shows the in situ monitoring of the powder evaporation for the 0.2 CsBr/1 PbI_2 case. In the first part of the measurement, from ambient temperature to 330 °C, a general shift of the diffraction peaks toward lower angles can be observed. It is caused by heating, resulting in a lattice expansion, as expected from materials with a positive thermal expansion coefficient. A phase rearrangement can be deduced from orientations increasing or decreasing in intensity, like the CsBr (100) peak close to 9° or the PbI_2 (102) peak close to 15°, respectively (with a beamline wavelength of 0.694 Å). Between 330 and 370 °C, a horizontal band can be observed. As displayed in the Supporting Information (Figure S4), in this temperature range, the maps feature needle-like shapes with orientations that are quickly changing. This is due to the coalescence of powder particles forming crystallites with defects and rapidly changing orientations. This rearrangement of matter continues until the temperature is high enough for evaporation. At this point, only the background from the glass capillary is detected. Interestingly, some new species can be detected close to the evaporation temperature. Prominently, a newly formed $PbBr_2$ phase is clearly distinguishable from the peak positions and the diffraction multiplicity, well below the evaporation temperature. Just above the transition to the evaporation regime, which results in a significant reduction in the signal-to-noise ratio, several other species appear. This is possibly pointing toward other (mixed/halide exchange) species such as $CsPbI_3$, Cs, or CsI, as indicated by the different symbols. However, given the signal-to-noise ratio for these peaks and the overlap of possible phases, their presence cannot be assessed with certainty. The halide substitution in the powder mixes follows a thermally activated, single-rate process, as can be seen in the Arrhenius plot of the clearly identified $PbBr_2$ peak close to evaporation, available in the Supporting Information (Figure S5). This demonstrates that halide exchange between the precursors takes place close to and during evaporation and points toward the possibility of actively tuning halide exchange and premelted mixes in the future. This calls to mind the molten salt approach of Li et al.[20] previously discussed in this manuscript, where they melted the mixed salts before usage. Rapid interfacial halide diffusion has also been studied in the case of stacked metal halide perovskite thin films by Hautzinger et al.[21] They show that spin coating $CsPbI_3$ nanocrystals on top of a formed $CsPbBr_3$ nanocrystal thin film (then annealing at 50 °C to remove the solvent) results in considerable halide interdiffusion, which can be prevented with single-layer graphene between the two inorganic perovskites. Single-source evaporation of mixed precursors is a very attractive technique due to its simplicity and rapidity, but the halide exchanges that may occur during the process must be taken into account. Future work should investigate this aspect of the process and the potential tuning leverage that it provides for compositional engineering.[22]

$Cs_xPbI_yBr_z$ Metal Halide Template Thin Films. The different powder mixtures were evaporated from a single source with our in-house thermal evaporator. For each single-source evaporation, 1 g of each mix was loaded into a precleaned and prebaked ceramic crucible and evaporated at a set, constant temperature (325, 350, and 375 °C). The evaporation temperatures were chosen based on our experience with the single powders, in order to satisfy the following compromise: the temperature has to be high enough to allow evaporation of both PbI_2 and CsBr and sufficiently low to ensure that the evaporation rate profile is controlled and repeatable. All powder mixes were evaporated targeting a 200 nm thin film, analogous to the coevaporated metal halide template used in our baseline. The pressure in the chamber was in the 10^{-6} mbar range.

https://doi.org/10.1021/acsphotonics.3c00438
ACS Photonics 2023, 10, 3087−3094

Figure 3a shows the two-dimensional diffraction pattern of a metal halide template obtained by evaporating the 0.2 powder mix. The measurement only shows the presence of PbI_2, with the (001) plane and its higher-order reflections detected with a strong preferential orientation at an azimuthal angle of 90 ± 10°. The latter result agrees with the nanoplatelets' arrangement predominantly oriented face up (with respect to the substrate) that is typically obtained when thermally evaporating PbI_2[23−25] and visible in the scanning electron microscope (SEM) image of the corresponding film in Figure 3b. The two diffraction wings on the sides stem from the substrate background. Measurement data of the other powder mixes and a coevaporated template are provided as the Supporting Information (Figure S6) and all feature the exact same characteristics: we observe no clearly distinguishable crystalline CsBr nor any other phase, but within the measured range, only a strong PbI_2 signal oriented perpendicular to the substrate.

As a complement to this structural information, quantification of the chemical composition was done using EDX, with the protocol described in the Methods section. Figure 4 compares the obtained Cs/Pb, Br/Pb, and Cs/Br ratios for thin films evaporated from different ball-milled powders and at different evaporation temperatures. The target ratios of 0.2414 Cs/Pb, 0.2476 Br/Pb, and 0.975 Cs/Br are defined by the values obtained in our coevaporated template baseline (see pure precursor materials before and after evaporation in the Supporting Information (Figure S7)). Thus, when depositing Cs and Br in the targeted stoichiometry (i.e., coevaporating CsBr and PbI_2 powders in dedicated crucibles), it results in a relatively close atomic ratio in the grown thin film. However, Figure 4 demonstrates that evaporating the mixed powders does not allow us to achieve the intended atomic ratios within the chosen experimental parameters (the Cs/Br ratios are comprised between 0.23 and 0.82 with a median value of 0.46, far from 0.975 of the coevaporated reference). This in turn suggests a species dissociation/halide exchange during the heating and single-source evaporation phase, in line with the in situ observed appearance of, e.g., $PbBr_2$. Different phenomena are happening at the same time. First, an increase in the CsBr/PbI_2 atomic ratio in the source increases the likelihood of a halide exchange. The latter, as discussed previously, follows a behavior described by the Arrhenius equation and is thus favored at higher temperatures. Higher temperatures also mean that more cesium halides are evaporated, but also a further increase in the evaporation rate of lead halides. Figure 4c shows the intricacy of this interplay.

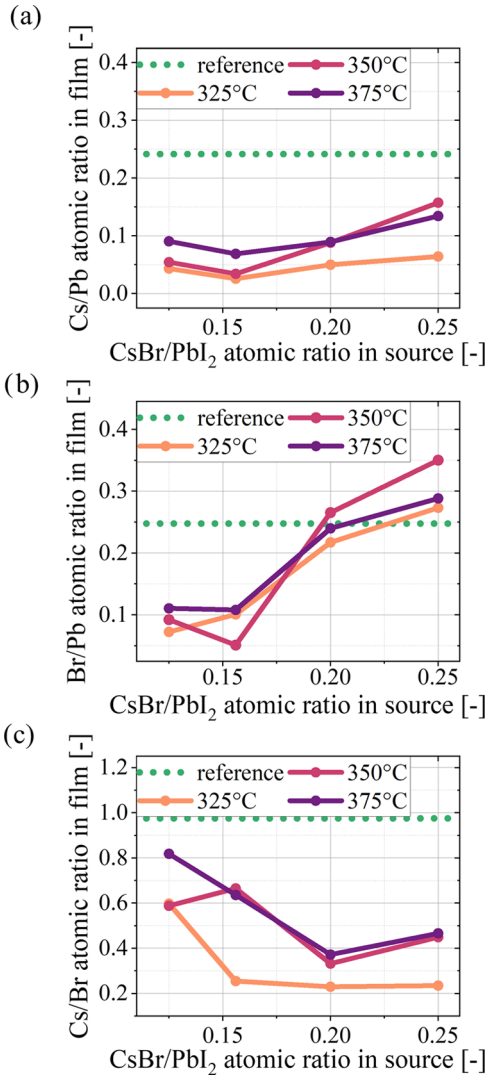

Figure 4. Chemical quantification of (a) Cs and (b) Br contents with respect to Pb in the single-source-evaporated thin films. (c) Corresponding Cs/Br ratios. Data obtained by EDX.

This halide exchange may be resolved by evaporating at a higher temperature and heating rate or flash evaporation. We chose not to seek this path due to setup limitations (insufficient heating capacity, i.e., evaporating substantial amounts of PbI_2 before reaching the set point) and deemed the approach less desirable since we expect that the ensuing vast evaporation rates would bring controllability/repeatability issues. Alternatively, we speculate that a more promising approach could be a partial replacement of CsBr with CsI in the powder mix. This would allow for increasing the amount of cesium in the resulting film while moderating the bromine content to reach the targeted relative amounts while ensuring reproducibility. Since these template films are converted into mixed organic−inorganic perovskite layers in a subsequent step, an alternative could be to accept an increased Br content in the template and tune the final iodine/bromine content with the organohalide deposition used for the conversion into a perovskite in the second step. Investigating the spatial distribution of chemical species after single-source evaporation is out of the scope of this study. However, the work of Moser et al.[26] shows that upon conversion into perovskite of a metal halide template, compositional gradients are homogenized. In their case, the initial template consisted of a bilayer of a pure PbI_2 layer on top of a pure CsI layer, and after conversion into a perovskite, Cs and Pb are homogeneously spread along the perovskite layer.

Template Conversion into Perovskites. The metal halide templates obtained by co- or single-source evaporation were converted into perovskite thin films by spin coating a formamidinium halide solution (1 FAI/2 FABr molar ratio, concentration: 0.46 M, in ethanol). The thin films were then annealed at 150 °C for 20 min in air with controlled humidity (30% RH).

Figure 5a shows the diffraction pattern as a function of the azimuthal angle of a converted template obtained by evaporation of the 0.2 powder mix. Note that we observed residual PbI_2, indicative of a mild underconversion. The identified phases demonstrate the presence of PbI_2, as well as

https://doi.org/10.1021/acsphotonics.3c00438
ACS Photonics 2023, 10, 3087−3094

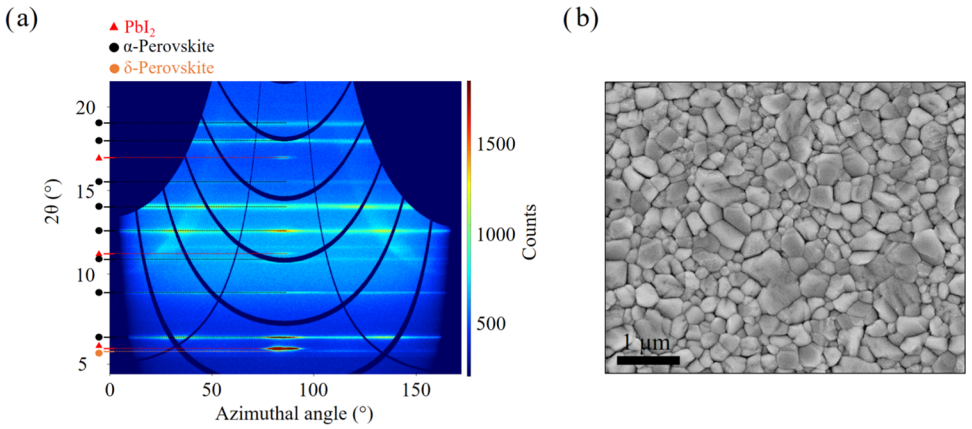

Figure 5. (a) Diffraction pattern as a function of the azimuthal angle of a partially converted metal halide template (from 0.2 powder mix evaporation) and (b) SEM top view of a randomly oriented perovskite obtained by evaporation of metal halide and then spin coating of organohalide.

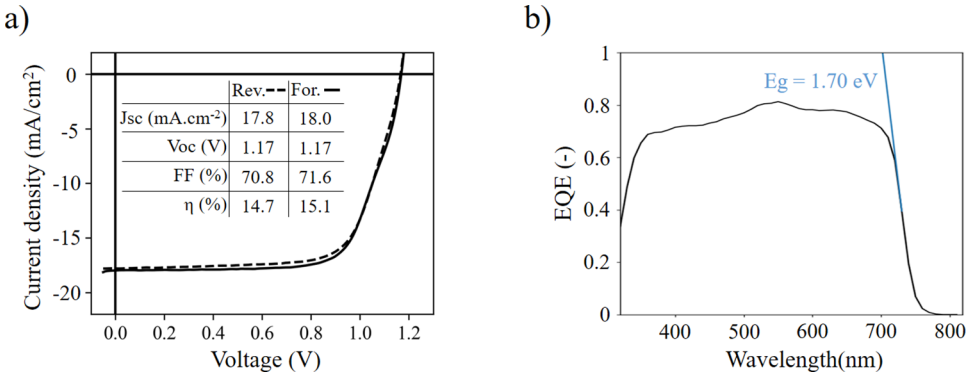

Figure 6. (a) Current density−voltage curve and parameters of the best proof-of-concept device and (b) corresponding external quantum efficiency.

cubic and hexagonal formamidinium-based perovskites. The perovskite phases show a certain preferential orientation with the faces of the cubic structure mostly centered around three azimuthal angles: 37, 90, and 143°. This is the result of perovskite crystals dominantly oriented face and corner up, perpendicular to the substrate.[27,28] When the conversion into a perovskite is completed, this translates into small and randomly oriented domains, as displayed in Figure 5b. The other converted perovskite film diffraction maps are provided in the Supporting Information (Figures S9 and S10), and they all display the same features. A notable exception is the films arising from the 0.25 powder mix templates, featuring a more pronounced presence of impurities such as hexagonal formamidinium perovskites and also a weak but distinguishable signal from the orthorhombic nonphotoactive phase of $CsPbI_3$. Groeneveld et al.[29] observed the same nonphotoactive impurities in their solution-processed thin films. Similarly, a small increase in bromine content ($Cs_{0.1}FA_{0.9}PbI_{3-x}Br_x$ with x increased from 0.45 to 0.6) was enough to have a detrimental effect on the purity and photoluminescence lifetime of the film. The appearance of such defects sets boundaries for the experimental space to be explored by the compositional engineering approach mentioned in previous sections.

Proof-of-concept photovoltaic devices were realized with the following architecture: glass/indium tin oxide/MeO-2PACz/perovskite/C_{60}/bathocuproine/silver. The metal halide templates obtained by single-source evaporation of the 0.20 and 0.25 powder mixes at 350 °C were chosen. This choice was motivated by it being the best compromise between the Cs/Pb and Pb/Br ratios relative to the coevaporated baseline (cf. Figure 4). Fortunately, these conditions also exhibited the most repeatable and controllable evaporation. The organohalide solution concentration was increased to maximize the conversion into perovskites and the performance. Figure 6 exhibits the main characteristics of the best proof-of-concept device. It reaches 15% efficiency with an absorber with an optical bandgap of 1.70 eV and is obtained with a 0.20 powder mix template converted by a 0.51 M organohalide solution. Devices fabricated with the 0.25 powder mix exhibit a much narrower range of "optimal performance" and are even in the best case less efficient (best device at 12%, statistics provided in the Supporting Information (Figure S11)). This can be explained by the increased amount of impurities in the film, as discussed previously, and a slightly higher optical bandgap of 1.72 eV, hence lower photocurrent, further away from the Shockley−Queisser optimum.

CONCLUSIONS

We investigated the mixing, single-source evaporation, and conversion into perovskites of nonstoichiometric PbI_2 and CsBr mixes. Although no new phase could be formed during the ball-milling of the precursors, new phases created by halide exchange were observed close to evaporation via in situ GIWAXS. This species rearrangement was confirmed by chemical analysis of the as-deposited thin films with EDX

https://doi.org/10.1021/acsphotonics.3c00438
ACS Photonics 2023, 10, 3087−3094

and shown to be favored by lower temperatures of evaporation. Consequently, we chose to compromise between a high evaporation rate and controllable/reproducible evaporation profiles. The conversion of the metal halide templates into formamidinium-based perovskites reveals a face and corner up, perpendicular to the substrate, favored orientation. It is found that films with an initially higher amount of CsBr promote the growth of nonphotoactive phases and thus lessen the photovoltaic device performances. In a future study, it would be interesting to study under which conditions mechanosynthesis techniques such as ball-milling can favor, or not, the appearance of new phases when mixing metal halides. In the case of strict mixing, without new phases, fine-tuning the final film composition by introducing new metal halides appears as an engaging path to follow.

METHODS

Characterization. Synchrotron X-ray diffraction was performed at the BM01 diffraction beamline of the Swiss-Norvegian Beamlines (SNBL) of the European Synchrotron Radiation Facility (ESRF) in Grenoble, France. The wavelength during the measurements was 0.694 Å. A Pilatus 2M2D detector was used.[30] For the in situ GIWAXS study of the powder evaporation, precursors were loaded in glass capillary tubes connected to a turbo pump, and a hot air blower was used to heat the capillary during the GIWAXS measurement. Different temperature ramps were tested from 6 to 24 °C/min without apparent changes in behavior. All data presented here were acquired using a 6 °C/min ramp. Secondary electron SEM images were acquired with an in-lens detector in a Zeiss Gemini 2 microscope. EDX quantification of thin films was obtained with the same system by averaging data from 15 different millimeter-sized areas taken across three different substrates from the same evaporation. Pb, Cs, Br, and I were fitted, and Si, N, Mg, Ca, O, Na, B, C, In, and Sn were deconvoluted (diverse backgrounds from the glass substrate covered by indium tin oxide). The resulting standard deviations were in the few percent range. Current density−voltage (J−V) measurements were performed using a two-lamp (halogen and xenon) class AAA WACOM sun simulator with an AM1.5G irradiance spectrum of 1000 $W.m^{-2}$. Shadow masks were used to define the illuminated area (0.1 cm^2), and the cells were measured with a scan rate of 100 $mV.s^{-1}$. External quantum efficiency (EQE) spectra were obtained using a custom-made spectral response setup with a lock-in amplifier using chopped light at a frequency of 232 Hz.

Thin-Film Processing. Precursors were mixed in a shaking mill at a frequency of 25 Hz for 1 h with agate grinding balls. Powders were evaporated in a Lesker Mini SPECTROS evaporation system. 1 g of each mix was loaded in a crucible, and the source was heated at a set point as fast as possible, then the shutter was opened, and the temperature was kept constant until the nominal thickness of 200 nm was reached. Evaporation rates ranged between 10 and 3 Å/s. The acoustic impedance, density, and tooling factor used for CsBr and PbI_2 in our system are the following, respectively: [1.41, 4.456, 22.8] and [0.11, 6.16, 19.9]. The accuracy of set, measured, and effective deposition rates is ensured by dedicated tuning of the tooling factor of each source for each type of material. The tooling factor is adequately determined after a single-material evaporation of a given compound by measuring the difference between the thickness measured by the QCM (with initial parameters of tooling factor, density, etc.) and the thickness of the film as determined by a combination of different tools: cross-sectional scanning electron microscope, profilometer, and ellipsometer. Conversion into perovskites was obtained by spin coating FAI/FABr (Greatcell) 1:2 dissolved in dry ethanol (Sigma-Aldrich) and then annealing the thin films at 150 °C for 20 min in ambient air 30% RH. MeO-2PACz (TCI) was dissolved in dry ethanol to form a 1 mg/mL solution, 100 μL was dispersed on the static sample, and then the sample was rotated to 3000 rpm, where 100 μL was anew dispersed on the film. The sample was then annealed at 100 °C for 10 min and then washed with dry ethanol. C_{60} (CreaPhys), bathocuproine, and silver (Sigma-Aldrich) were thermally evaporated in high vacuum in a dedicated chamber with the following rates/thicknesses, respectively: 0.2 Å/s/20 nm, 0.2 Å/s/5 nm, and 1.5 Å/s/130 nm.

ASSOCIATED CONTENT

Supporting Information

The Supporting Information is available free of charge at https://pubs.acs.org/doi/10.1021/acsphotonics.3c00438.

Additional powder diffractograms, schematic of the GIWAXS setup, additional in situ powder diffractograms, additional Arrhenius analysis of the PbBr2 peak evolution, additional scanning electron microscopy images, additional solar cell performance data, and comparison of XRF and EDX quantification in pages S1−S11 and figures S1−S11 (PDF)

AUTHOR INFORMATION

Corresponding Authors

Quentin Guesnay − *Ecole Polytechnique Fédérale de Lausanne (EPFL), Institute of Electrical and Microengineering (IEM), Photovoltaics and Thin-Film Electronics Laboratory, Neuchâtel 2002, Switzerland*; Email: quentin.guesnay@epfl.ch

Christian M. Wolff − *Ecole Polytechnique Fédérale de Lausanne (EPFL), Institute of Electrical and Microengineering (IEM), Photovoltaics and Thin-Film Electronics Laboratory, Neuchâtel 2002, Switzerland*; orcid.org/0000-0002-7210-1869; Email: christian.wolff@epfl.ch

Authors

Charles J. McMonagle − *Swiss-Norwegian Beamlines, European Synchrotron Radiation Facility, Grenoble 38000, France*

Dmitri Chernyshov − *Swiss-Norwegian Beamlines, European Synchrotron Radiation Facility, Grenoble 38000, France*; orcid.org/0000-0001-7738-9358

Waqas Zia − *Institute for Photovoltaics (ipv), University of Stuttgart, Stuttgart 70569, Germany; IEK5-Photovoltaics, Forschungszentrum Jülich, Jülich 52428, Germany*

Alexander Wieczorek − *Laboratory for Surface Science and Coating Technologies, Empa−Swiss Federal Laboratories for Materials Science and Technology, Duebendorf 8600, Switzerland*; orcid.org/0000-0002-1025-128X

Sebastian Siol − *Laboratory for Surface Science and Coating Technologies, Empa−Swiss Federal Laboratories for Materials Science and Technology, Duebendorf 8600, Switzerland*; orcid.org/0000-0002-0907-6525

Michael Saliba − *Institute for Photovoltaics (ipv), University of Stuttgart, Stuttgart 70569, Germany; IEK5-Photovoltaics,*

Forschungszentrum Jülich, Jülich 52428, Germany; orcid.org/0000-0002-6818-9781

Christophe Ballif − *Ecole Polytechnique Fédérale de Lausanne (EPFL), Institute of Electrical and Microengineering (IEM), Photovoltaics and Thin-Film Electronics Laboratory, Neuchâtel 2002, Switzerland; CSEM, Sustainable Energy Center, Neuchâtel 2000, Switzerland*

Complete contact information is available at: https://pubs.acs.org/10.1021/acsphotonics.3c00438

Funding

The authors thank the Swiss National Science Foundation (SNSF) (Papet, 200021_197006), the ETH board (AMYS), SNSF Bridge Discovery (A3P, 40B2-0_1203626), the Swiss Federal Office of Energy (Presto), and Horizon 2020 (Texta, 101033077, MSCA-IF-2020, CMW) for funding. MS and WZ thank the Helmholtz Young Investigator Group FRONT-RUNNER. M.S. thanks the German Research Foundation (DFG) for funding (SPP2196, 431314977/GRK 2642). M.S. acknowledges funding by ProperPhotoMile. Project Proper-PhotoMile is supported under the umbrella of SOLAR-ERA.NET co-funded by The Spanish Ministry of Science and Education and the AEI under Project PCI2020-112185 and CDTI Project IDI-20210171; the Federal Ministry for Economic Affairs and Energy based on a decision by the German Bundestag Projects FKZ 03EE1070B and FKZ 03EE1070A and the Israel Ministry of Energy with Project 220-11-031. SOLAR-ERA.NET is supported by the European Commission within the EU Framework Programme for Research and Innovation HORIZON 2020 (Cofund ERA-NET action number 786483) funded by the European Union. M.S. acknowledges funding from the European Research Council under the Horizon Europe program (LOCAL-HEAT, Grant Agreement 101041809). M.S. acknowledges funding from the German Bundesministerium für Bildung and Forschung (BMBF), project "NETPEC" (01LS2103E).

Notes

The authors declare no competing financial interest.

REFERENCES

(1) Borchert, J.; Milot, R. L.; Patel, J. B.; Davies, C. L.; Wright, A. D.; Martínez Maestro, L.; Snaith, H. J.; Herz, L. M.; Johnston, M. B. Large-Area, Highly Uniform Evaporated Formamidinium Lead Triiodide Thin Films for Solar Cells. *ACS Energy Lett.* **2017**, *2*, 2799−2804.

(2) Luo, L.; Zhang, Y.; Chai, N.; Deng, X.; Zhong, J.; Huang, F.; Peng, Y.; Ku, Z.; Cheng, Y.-B. Large-area perovskite solar cells with Cs x FA 1x PbI 3y Br y thin films deposited by a vapor−solid reaction method. *J. Mater. Chem. A* **2018**, *6*, 21143−21148.

(3) Qiu, L.; He, S.; Jiang, Y.; Son, D.-Y. Y.; Ono, L. K.; Liu, Z.; Kim, T.; Bouloumis, T.; KAZAOUI, S.; Qi, Y. Hybrid Chemical Vapor Deposition Enables Scalable and Stable Cs-FA Mixed Cation Perovskite Solar Modules with a Designated Area of 91.8 cm2 Approaching 10% Efficiency. *J. Mater. Chem. A* **2019**, *7*, 6920−6929.

(4) Roß, M.; Severin, S.; Stutz, M. B.; Wagner, P.; Köbler, H.; Favin-Lévêque, M.; Al-Ashouri, A.; Korb, P.; Tockhorn, P.; Abate, A.; Stannowski, B.; Rech, B.; Albrecht, S. Co-Evaporated Formamidinium Lead Iodide Based Perovskites with 1000 h Constant Stability for Fully Textured Monolithic Perovskite/Silicon Tandem Solar Cells. *Adv. Energy Mater.* **2021**, *11*, 2101460.

(5) Feng, J.; Jiao, Y.; Wang, H.; Zhu, X.; Sun, Y.; Du, M.; Cao, Y.; Yang, D.; Liu, S. F. High-throughput large-area vacuum deposition for high-performance formamidine-based perovskite solar cells. *Energy Environ. Sci.* **2021**, *14*, 3035−3043.

(6) Guesnay, Q.; Sahli, F.; Ballif, C.; Jeangros, Q. Vapor deposition of metal halide perovskite thin films: Process control strategies to shape layer properties. *APL Mater.* **2021**, *9*, 100703.

(7) Held, V.; Mrkyvkova, N.; Nádaždy, P.; Vegso, K.; Vlk, A.; Ledinský, M.; Jergel, M.; Chumakov, A.; Roth, S. V.; Schreiber, F.; Siffalovic, P. Evolution of Structure and Optoelectronic Properties during Halide Perovskite Vapor Deposition. *J. Phys. Chem. Lett.* **2022**, *13*, 11905−11912.

(8) Qin, M.; Chan, P. F.; Lu, X. A Systematic Review of Metal Halide Perovskite Crystallization and Film Formation Mechanism Unveiled by In Situ GIWAXS. *Adv. Mater.* **2021**, *33*, 2105290.

(9) Sahli, F.; Werner, J.; Kamino, B. A.; et al. Fully textured monolithic perovskite/silicon tandem solar cells with 25.2% power conversion efficiency. *Nat. Mater.* **2018**, *17*, 820−826.

(10) Igual-Muñoz, A. M.; Navarro-Alapont, J.; Dreessen, C.; Palazon, F.; Sessolo, M.; Bolink, H. J. Room-Temperature Vacuum Deposition of CsPbI2Br Perovskite Films from Multiple Sources and Mixed Halide Precursors. *Chem. Mater.* **2020**, *32*, 8641−8652.

(11) Rodkey, N.; Kaal, S.; Sebastia-Luna, P.; Birkhölzer, Y. A.; Ledinsky, M.; Palazon, F.; Bolink, H. J.; Morales-Masis, M. Pulsed Laser Deposition of Cs2AgBiBr6: From Mechanochemically Synthesized Powders to Dry, Single-Step Deposition. *Chem. Mater.* **2021**, *33*, 7417−7422.

(12) Protesescu, L.; Yakunin, S.; Nazarenko, O.; Dirin, D. N.; Kovalenko, M. V. Low-Cost Synthesis of Highly Luminescent Colloidal Lead Halide Perovskite Nanocrystals by Wet Ball Milling. *ACS Appl. Nano Mater.* **2018**, *1*, 1300−1308.

(13) El Ajjouri, Y.; Igual-Muñoz, A. M.; Sessolo, M.; Palazon, F.; Bolink, H. J. Tunable Wide-Bandgap Monohalide Perovskites. *Adv. Opt. Mater.* **2020**, *8*, No. 2000423.

(14) Tang, S.; Xiao, X.; Hu, J.; Gao, B.; Chen, H.; Zuo, Z.; Qi, Q.; Peng, Z.; Wen, J.; Zou, D. Mechanochemical synthesis of pure phase mixed-cation/anion (FAPbI3)x(MAPbBr3)1xhybrid perovskite materials: compositional engineering and photovoltaic performance. *RSC Adv.* **2021**, *11*, 5874−5884.

(15) López, C. A.; Alvarez-Galván, M. C.; Martínez-Huerta, M. V.; Fauth, F.; Alonso, J. A. Crystal structure features of CH3NH3PbI3-: XBrx hybrid perovskites prepared by ball milling: A route to more stable materials. *CrystEngComm* **2020**, *22*, 767−775.

(16) Palazon, F.; El Ajjouri, Y.; Sebastia-Luna, P.; Lauciello, S.; Manna, L.; Bolink, H. J. Mechanochemical synthesis of inorganic halide perovskites: Evolution of phase-purity, morphology, and photoluminescence. *J. Mater. Chem. C* **2019**, *7*, 11406−11410.

(17) Bette, S.; Takayama, T.; Kitagawa, K.; Takano, R.; Takagi, H.; Dinnebier, R. E. Solution of the heavily stacking faulted crystal structure of the honeycomb iridate H3LiIr2O6. *Dalton Trans.* **2017**, *46*, 15216−15227.

(18) Palosz, B. The structure of PbI2 polytypes 2H and 4H: A study of the 2H-4H transition. *J. Phys.: Condens. Matter* **1990**, *2*, 5285−5295.

(19) Beckmann, P. A. A review of polytypism in lead iodide. *Cryst. Res. Technol.* **2010**, *45*, 455−460.

(20) Li, H.; Tan, L.; Jiang, C.; Li, M.; Zhou, J.; Ye, Y.; Liu, Y.; Yi, C. Molten Salt Strategy for Reproducible Evaporation of Efficient Perovskite Solar Cells. *Adv. Funct. Mater.* **2023**, *33*, 2211232.

(21) Hautzinger, M. P.; Raulerson, E. K.; Harvey, S. P.; Liu, T.; Duke, D.; Qin, X.; Scheidt, R. A.; Wieliczka, B. M.; Phillips, A. J.; Graham, K. R.; Blum, V.; Luther, J. M.; Beard, M. C.; Blackburn, J. L. Metal Halide Perovskite Heterostructures: Blocking Anion Diffusion with Single-Layer Graphene. *J. Am. Chem. Soc.* **2023**, *145*, 2052−2057.

(22) Er-raji, O.; Rustam, L.; Kore, B. P.; Glunz, S. W.; Schulze, P. S. C. Insights into Perovskite Film Formation Using the Hybrid Evaporation/Spin-Coating Route: An In Situ XRD Study. *ACS Appl. Energy Mater.* **2023**, *6*, 6183−6193.

(23) Fu, F.; Kranz, L.; Yoon, S.; Löckinger, J.; Jäger, T.; Perrenoud, J.; Feurer, T.; Gretener, C.; Buecheler, S.; Tiwari, A. N. Controlled growth of PbI2 nanoplates for rapid preparation of CH3NH3PbI3 in

planar perovskite solar cells. *Phys. Status Solidi A* **2015**, *212*, 2708−2717.
(24) Koffman-Frischknecht, A.; Soldera, M.; Soldera, F.; Troviano, M.; Carlos, L.; Perez, M. D.; Taretto, K. Tuning morphological features of lead iodide by low pressure vapor phase deposition. *Thin Solid Films* **2018**, *653*, 249−257.
(25) Hu, H.; Wang, D.; Zhou, Y.; Zhang, J.; Lv, S.; Pang, S.; Chen, X.; Liu, Z.; Padture, N. P.; Cui, G. Vapour-based processing of hole-conductor-free CH3NH 3PbI3 perovskite/C60 fullerene planar solar cells. *RSC Adv.* **2014**, *4*, 28964−28967.
(26) Moser, T.; Kothandaraman, R.; Yang, S.; Walter, A.; Siegrist, S.; Lai, H.; Gilshtein, E.; Tiwari, A. N.; Fu, F. Understanding the Formation Process of Perovskite Layers Grown by Chemical Vapour Deposition. *Front. Energy Res.* **2022**, *10*, No. 883882.
(27) Oesinghaus, L.; Schlipf, J.; Giesbrecht, N.; Song, L.; Hu, Y.; Bein, T.; Docampo, P.; Müller-Buschbaum, P. Toward Tailored Film Morphologies: The Origin of Crystal Orientation in Hybrid Perovskite Thin Films. *Adv. Mater. Interfaces* **2016**, *3*, No. 1600403.
(28) Wang, L.; Wang, X.; Zhu, L.; Leng, S. B.; Liang, J.; Zheng, Y.; Zhang, Z.; Zhang, Z.; Liu, X. X.; Liu, F.; Chen, C. C. Favorable grain growth of thermally stable formamidinium-methylammonium perovskite solar cells by hydrazine chloride. *Chem. Eng. J.* **2022**, *430*, 132730.
(29) Groeneveld, B. G. H. M.; Adjokatse, S.; Nazarenko, O.; Fang, H. H.; Blake, G. R.; Portale, G.; Duim, H.; ten Brink, G. H.; Kovalenko, M. V.; Loi, M. A. Stable Cesium Formamidinium Lead Halide Perovskites: A Comparison of Photophysics and Phase Purity in Thin Films and Single Crystals. *Energy Technol.* **2020**, *8*, 1901041.
(30) Dyadkin, V.; Pattison, P.; Dmitriev, V.; Chernyshov, D. A new multipurpose diffractometer PILATUS@SNBL. *J. Synchrotron Radiat.* **2016**, *23*, 825−829.

https://doi.org/10.1021/acsphotonics.3c00438
ACS Photonics 2023, 10, 3087−3094